ACS APPLIED MATERIALS & INTERFACES

Research Article

www.acsami.org

Contribution of Energetically Reactive Surface Features to the Dissolution of CeO_2 and ThO_2 Analogues for Spent Nuclear Fuel Microstructures

Claire L. Corkhill,*[,†] Emmi Myllykylä,[‡] Daniel J. Bailey,[†] Stephanie M. Thornber,[†] Jiahui Qi,[§] Pablo Maldonado,[∥] Martin C. Stennett,[†] Andrea Hamilton,[⊥] and Neil C. Hyatt*[,†]

[†]Immobilisation Science Laboratory, Department of Materials Science and Engineering, The University of Sheffield, Sheffield S1 3JD, United Kingdom

[‡]VTT Technical Research Centre of Finland, Espoo FI-02044, Finland

[§]Royal School of Mines, Imperial College London, London SW7 2AZ, United Kingdom

[∥]Department of Physics and Astronomy, Uppsala Universitet, 751 05 Uppsala, Sweden

[⊥]Department of Civil and Environmental Engineering, The University of Strathclyde, Glasgow G1 1XQ, United Kingdom

ABSTRACT: In the safety case for the geological disposal of nuclear waste, the release of radioactivity from the repository is controlled by the dissolution of the spent fuel in groundwater. There remain several uncertainties associated with understanding spent fuel dissolution, including the contribution of energetically reactive surface sites to the dissolution rate. In this study, we investigate how surface features influence the dissolution rate of synthetic CeO_2 and ThO_2, spent nuclear fuel analogues that approximate as closely as possible the microstructure characteristics of fuel-grade UO_2 but are not sensitive to changes in oxidation state of the cation. The morphology of grain boundaries (natural features) and surface facets (specimen preparation-induced features) was investigated during dissolution. The effects of surface polishing on dissolution rate were also investigated. We show that preferential dissolution occurs at grain boundaries, resulting in grain boundary decohesion and enhanced dissolution rates. A strong crystallographic control was exerted, with high misorientation angle grain boundaries retreating more rapidly than those with low misorientation angles, which may be due to the accommodation of defects in the grain boundary structure. The data from these simplified analogue systems support the hypothesis that grain boundaries play a role in the so-called "instant release fraction" of spent fuel, and should be carefully considered, in conjunction with other chemical effects, in safety performance assessements for the geological disposal of spent fuel. Surface facets formed during the sample annealing process also exhibited a strong crystallographic control and were found to dissolve rapidly on initial contact with dissolution medium. Defects and strain induced during sample polishing caused an overestimation of the dissolution rate, by up to 3 orders of magnitude.

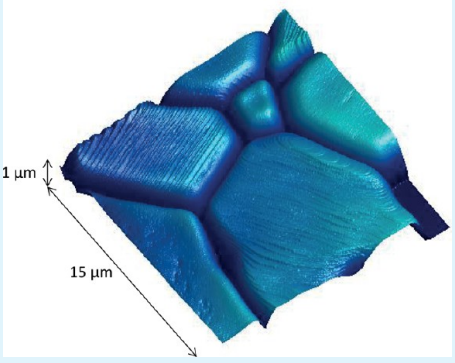

KEYWORDS: *nuclear fuel, dissolution, grain boundaries, faceting, surface, atomic force microscopy*

1. INTRODUCTION

Spent nuclear fuel is a heterogeneous material composed primarily of UO_2, with a minor component of actinides (e.g., Np and Pu) and fission products (e.g., Sr, Cs, and I). The preferred route for disposal of this material is within a geological disposal facility, several hundreds of meters below the ground. In such an environment, the release of radionuclides to the geo- and biospheres is controlled by the dissolution of the spent fuel in groundwater; thus it is important to understand the mechanisms and kinetics of dissolution. The dissolution behavior of spent fuel is dominated by the behavior of the UO_2 matrix, and, as such, a simplified system comprising UO_2 only is often used in experiments to determine SNF dissolution. On the basis of a wide range of dissolution investigations of SNF and UO_2 (see reviews[1,2]), it has been estimated that the fractional dissolution rate of spent nuclear fuel is in the range of 10^{-6} to 10^{-8} per year, indicating that complete dissolution is likely to occur within ~10 million years.[3] However, natural uraninite (UO_2) ores are known to be stable in the earth under reducing conditions for periods of billions of years,[4,5] suggesting that laboratory experiments may overestimate the dissolution rate of UO_2 by more than 2 orders of magnitude.

It has been demonstrated that experimentally derived dissolution rates of other minerals, such as quartz and feldspar, are also often found to be higher than the corresponding weathering rate of the rocks they comprise.[6−9] One of the causes of this observed behavior is specimen preparation within

Received: March 28, 2014
Accepted: July 7, 2014
Published: July 7, 2014

the laboratory; the act of crushing generates sharp edges and other surface defects, and the atoms on the surface associated with these features have high surface energy and contain fewer chemical bonds than the atoms on defect-free surfaces, which, in turn, contain fewer chemical bonds than atoms within the bulk. Defect surfaces are removed during dissolution, leaving a lower energy surface that dissolves at a slower rate.[10,11] Knauss and Wolery[6] observed that the dissolution rate of crushed albite decreased during the first 20 days by over an order of magnitude in all experimental conditions. Similarly, during sequential leaching from 52 to 114 days, crushed UO_2 samples showed progressively decreasing dissolution rates.[12,13] Natural defects present at the surface have also been shown to affect dissolution rates; for example, Claparede et al.[14] found that crystal defects and initial crystallite size of mixed cerium–neodymium oxides influenced the dissolution rate.

To evidence the influence of high energy surface features on the dissolution rate of UO_2, CeO_2 and ThO_2 analogues are investigated. These materials were chosen because they are isostructural to UO_2 but are not sensitive to changes in oxidation state of the cation. Previously, we have synthesized CeO_2 and ThO_2 to closely resemble the microstructure of SNF;[15,16] therefore, we also make an assessment of how these physical and structural features are likely to influence the dissolution of SNF. Using an integrated approach, applying atomic force microscopy, vertical scanning interferometry, electron backscatter diffraction, and aqueous geochemical analysis, we determine how natural and specimen-induced high-energy surface sites (grain boundaries and surface defects, respectively) contribute to measured laboratory dissolution rates. Through this methodology, we aim to reduce the uncertainties associated with UO_2 dissolution, and thus improve our understanding of the relationship between laboratory studies and the dissolution rates to be expected under geological disposal conditions.

2. EXPERIMENTAL SECTION

2.1. CeO_2 and ThO_2 Preparation. Cerium dioxide monoliths were prepared according to Stennett et al.[15] Monoliths were ground and polished to a 0.05 μm finish using SiC paper and diamond paste. To develop a grain boundary structure at the surface of some of the monoliths, thermal annealing was conducted. Monoliths were heated to 1500 °C at a ramp rate of 5 °C min^{-1} and held for 1 min to develop a grain boundary texture. The final microstructure (equiaxed grains ranging in size from 10 to 30 μm and randomly orientated) was in good agreement with those published for UO_2 and SIMFUEL.[17,18] An area was masked with an inert glue to act as a nonreactive reference surface of constant height during the dissolution experiments.

ThO_2 powder (British Drug Houses Ltd., lot number G83757/541012) was used to prepare sintered ThO_2 monoliths. Briefly, 1 g of powder was uniaxially pressed in a 10 mm diameter hardened stainless steel die with a load of 100 MPa. Monoliths were sintered for 4 h at 1750 °C in a standard air atmosphere muffle furnace, at a ramp rate of 5 °C min^{-1}, which gave a final density of >94% of the theoretical density of ThO_2 (10.00 g m^{-3}), determined using the Archimedes method. Monoliths were ground and polished to a 0.25 μm finish using SiC paper and diamond paste. It was found that a final polishing step using a 0.06 μm silica colloid solution was required to obtain surfaces flat enough for analysis by electron back scatter diffraction (EBSD)[19] and by atomic force microscopy (AFM) (for ThO_2, only data, not images, are given in the text due to complexities associated with surface polishing). Grain boundaries were defined by heating to 1500 °C at a ramp rate of 5 °C min^{-1}. The resulting grains ranged in size from 5–30 μm, and grains were found to be randomly orientated, consistent with UO_2 and SIMFUEL microstructure.

2.2. Dissolution Experiments. CeO_2 and ThO_2 are insoluble materials; hence, they are difficult to dissolve without the application of aggressive conditions. As such, dissolution was performed at high temperature (90 and 150 °C) and in acidic media. All solutions were prepared using ultrahigh quality (UHQ) water (18 MΩ). The following dissolution experiments were conducted: (1) annealed CeO_2 and ThO_2 dissolution at 90 °C in 0.01 M HNO_3; (2) annealed CeO_2 dissolution at 150 °C in 0.01 M HNO_3; (3) annealed CeO_2 dissolution at room temperature in 0.01, 0.1, 1.5, 3, and 15 M HNO_3; (4) annealed CeO_2 dissolution at room temperature in a series of etching solutions (72 h in UHQ water, 15 h in 0.001 M HCl, 4 h in 0.01 M HCl); and (5) polished (i.e., not annealed to define grain texture) CeO_2 dissolution at 90 and 150 °C in 0.01 M HNO_3.

Dissolution experiments performed at 90 °C were conducted within 50 mL PTFE vessels, cleaned according to the ASTM PCT standard.[20] A single monolith of CeO_2 or ThO_2 was placed into a PTFE basket within the vessel, to allow contact of the whole monolith with the dissolution medium, and 40 mL of 0.01 M HNO_3 was added. Triplicate samples and duplicate blanks (containing no monolith) were placed in a Carbolite oven at 90 (±0.5) °C and sampled at 0, 1, 3, 7, 14, 21, 28, and 35 days. An aliquot (1.2 mL) of each sample was removed for aqueous elemental analysis. One monolith from each triplicate experiment was removed for surface characterization at each sampling point, and returned to the dissolution medium after analysis. Dissolution experiments performed at 150 °C were conducted in customized reactors, consisting of 3 mL PTFE inserts with a PTFE lid (cleaned as above), within a sealed steel pressure vessel. These were placed within a heating block, where the temperature was maintained at 150 (±1) °C. Monoliths were placed on PTFE inserts to ensure contact of the whole monolith with the dissolution medium, and 2 mL of 0.01 M HNO_3 was added. Experiments were destructively sampled at 1, 3, 7, 21, and 35 days, at which times the monoliths were subject to surface analysis and aqueous solutions were collected for elemental analysis. Dissolution experiments conducted at room temperature were performed within an atomic force microscopy (AFM) fluid cell containing a fragment of a CeO_2 monolith cut using a diamond slow saw, immersed within 3 mL of reaction medium.

2.3. Surface and Aqueous Analysis. Monolith surfaces and cross sections were imaged using a JEOL JSM6400 scanning electron microscope (SEM) operating with an accelerating voltage of 15 kV and a working distance of 18 mm. Analysis of crystallographic orientation was performed using electron backscatter diffraction (EBSD) (Oxford Instruments, Abingdon, Oxfordshire, UK) in conjunction with an FEI Sirion field emission SEM. EBSD maps of 100 μm^2 were obtained at an accelerating voltage of 20 kV and with a 0.25 μm step size, and analyzed using HKL Channel 5 software (Oxford Instruments). Surface topography was measured using vertical scanning interferometry (VSI) (Sensofar PLu2300 profilometer) using a confocal lens with 50× and 150× magnification, a numerical aperture of 0.95, and lateral and vertical resolutions of 111 and 1 nm, respectively. Changes in surface morphology during dissolution were also measured using atomic force microscopy (AFM); ex situ measurements were performed using a Veeco Dimension 3100 microscope, operating in tapping mode and using high aspect ratio AFM tips, and in situ measurements were conducted using a Digital Instruments Multimode/Nanoscope IIIa in contact mode. Aqueous elemental analysis of Ce was undertaken by inductively coupled plasma-mass spectroscopy (ICP-MS) using an Aglient 4500 spectrometer, and analysis of Th was performed using high-resolution ICP-MS (Element 2, ThermoScientific). Prior to analyses, all samples were acidified with 20 μL of concentrated HNO_3 to keep all elements dissolved in solution. Solution data are expressed as the normalized elemental leaching N_L(Ce, Th) (g m^{-2}) according to

$$N_L(\mathrm{Ce, Th}) = \frac{m_{\mathrm{Ce,Th}}}{S/V} \quad (1)$$

where $m_{Ce, Th}$ is the total amount of Ce or Th released into solution and S/V is the surface area to volume ratio. The normalized element leaching rate R_L(Ce, Th) (g m^{-2} d^{-1}) is determined by

$$R_L(\mathrm{Ce,\ Th}) = \frac{m_{\mathrm{Ce,Th}}}{\frac{S}{V} \times \Delta t} \quad (2)$$

where Δt is the leaching time in days.

3. RESULTS

3.1. CeO_2 and ThO_2 Dissolution Rate. The aqueous dissolution rate data derived from all experiments are given in Table 1. The dissolution rate for CeO_2 dissolved at 150 °C was $(6.34 \pm 0.1) \times 10^{-3}$ g m^{-2} d^{-1}; data are shown in Figure 1a. The initial dissolution rates, between 0 and 7 days, appeared to be more rapid than those between 7 and 35 days (Figure 1a), which may be due to solution saturation effects. Under the same dissolution conditions, but at 90 °C, the dissolution rate was significantly lower, at $(7.26 \pm 0.2) \times 10^{-5}$ g m^{-2} d^{-1}, but the same trend was found, with an initial, rapid dissolution followed by a slower dissolution from 7 to 35 days (Figure 1b, Table 1). Dissolution of ThO_2 exhibited behavior different from that of CeO_2, as shown in Figure 1c. At 90 °C, the dissolution was initially rapid (between 0 and 7 days, Figure 1c) at a rate of $(6.71 \pm 0.5) \times 10^{-5}$ g m^{-2} d^{-1}, but subsequently the dissolution rate significantly decreased, giving an overall rate between 0 and 28 days of $(5.23 \pm 0.1) \times 10^{-7}$ g m^{-2} d^{-1} (Table 1). Rapid dissolution could result from the release of material from high energy surface sites at the ThO_2 surface, leading to saturation of the solution with respect to Th, to a point at which amorphous $ThO_x(OH)_y \cdot H_2O$ or even polynuclear $Th_x(OH)_y$ species form. These amorphous phases are known to be capable of recrystallizing; for example, Rai et al.[21] showed that $ThO_{2(am)}$ converted to crystalline $ThO_{2(cr)}$ upon heating at 90 °C in acidic solution. Therefore, recrystallized ThO_2 may be able to form a protective layer on the surface of ThO_2, providing a barrier to further dissolution and giving rise to the dissolution behavior observed in Figure 1c.

Table 1. Dissolution Rates for CeO_2 and ThO_2 Samples Dissolved in 0.01 M HNO_3 as a Function of Specimen Preparation and Temperature[a]

specimen preparation	temp (°C)	rate (g m^{-2} d^{-1})
annealed CeO_2	90	$(7.26 \pm 0.2) \times 10^{-5}$
	150	$(6.34 \pm 0.1) \times 10^{-3}$
annealed ThO_2	90	$(5.23 \pm 0.1) \times 10^{-7}$
polished CeO_2	90	$(7.40 \pm 0.2) \times 10^{-2}$
	150	$(7.01 \pm 0.2) \times 10^{-2}$

[a]Errors given are the standard deviation of triplicate experiments.

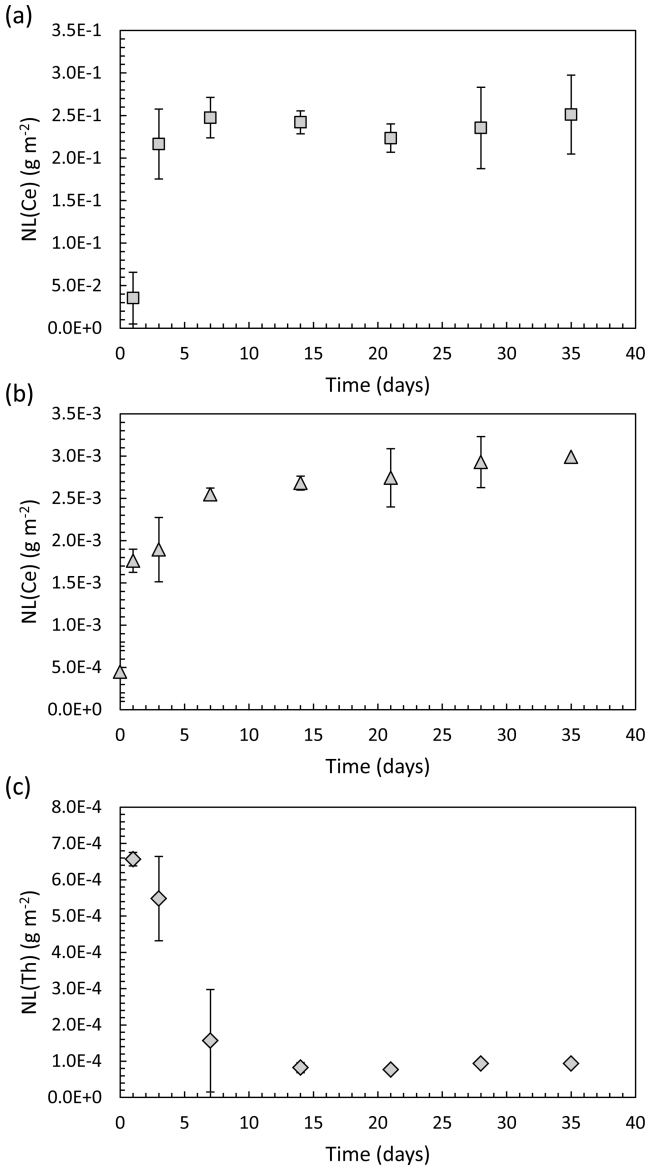

Figure 1. Normalized mass loss data for CeO_2 and ThO_2 dissolved in 0.01 M HNO_3: (a) annealed CeO_2 at 150 °C; (b) annealed CeO_2 at 90 °C; and (c) annealed ThO_2 at 90 °C. Errors given are the standard deviation of triplicate experiments. Corresponding dissolution rates are shown in Table 1.

3.2. Grain Boundaries. Grain boundaries are a well-known feature of SNF; they typically contain volatile fission products (e.g., Cs and I) and alloy particles of Mo, Tc, Ru, Rh, and Pd.[22] The presence of these highly radioactive elements necessitates a careful understanding of how grain boundaries behave during dissolution, and an evaluation of their contribution to the dissolution rate of spent fuel. Figure 2 shows the typical microstructure obtained for CeO_2; annealing conditions were optimized to give grain boundary depths of <1 μm.

The contribution of grain boundary dissolution to the overall dissolution rate of CeO_2 and ThO_2 was investigated in 0.01 M HNO_3 at 90 °C, and also at 150 °C for CeO_2. Figure 3 shows VSI images of CeO_2 before dissolution (Figure 3a) and after 3 and 7 days of dissolution at 150 °C (Figure 3b and c, respectively). It was found that after 3 days, dissolution was focused at grain boundaries and the pores between grains (Figure 3b). After 7 days, grain boundaries were preferentially dissolved, up to a depth of at least 0.70 μm, and the surface of the grains became rough and pitted (Figure 3c). Some of the grains dissolved at different rates, as evidenced by the height contrast in different grains (Figure 3b,c). In their analysis of CaF_2 dissolution (isostructural to CeO_2, ThO_2, and UO_2), Godinho et al.[23] showed that the measured retreat rates of CaF_2 grains depended upon the crystallographic orientation of the exposed planes. They concluded that the {111} plane is the most stable and dissolved most slowly, while the {112} plane was the least stable, dissolving up to 33 times faster than {111}. First-principles calculations have shown that the surface stability of CeO_2 from the most to the least stable plane is in the order of {111} > {110} > {100},[24,25] although it should be noted that the {100} plane in such calculations is modeled and not real, due to the difficulties associated with modeling the dipolar {100} plane. The results presented here are in

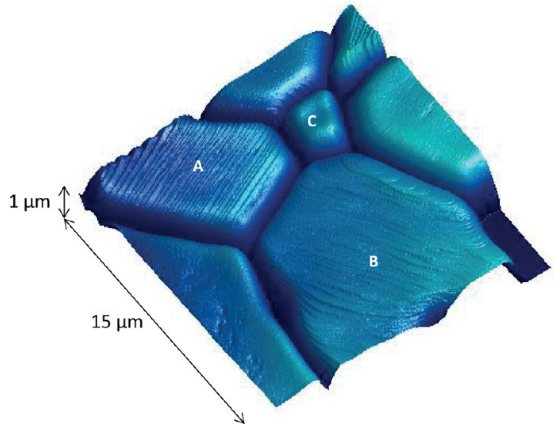

Figure 2. AFM image of CeO_2 surface, showing grains, grain boundaries, pores, and facets. The labels A, B, and C correspond to detailed analysis of grain facets, where A shows facets generated through the intersection of {665}/{$\bar{1}$11} planes, B shows facets generated through the intersection of {111}/{$\bar{1}$11} planes, and C shows no facets.

agreement with these findings; EBSD analysis of the grains in Figure 3c showed that the most stable grain had a (111) surface.

Figure 3d shows an SEM image of CeO_2 after 21 days of dissolution. The grains became entirely detached from the surface and were considerably smaller than their original size prior to dissolution (~5 μm, as compared to an initial size of 10–30 μm). The images in Figure 3 indicate that dissolution occurs preferentially along the grain boundaries, such that intergranular bonding becomes weakened with ongoing dissolution, eventually resulting in grain boundary decohesion. It is notable that the detached grains in Figure 3d exhibit triangular facets, indicative of {111} plane terminations, suggesting that surfaces that dissolve more slowly are the most stable, and persist during dissolution. Evidence for grain boundary decohesion in CeO_2 under these dissolution conditions was confirmed by SEM analysis of monoliths in cross section, with the surface of the grain just above the field of view. Figure 4a shows the cross section of a pristine, annealed sample of CeO_2. Grain boundaries were not observed in the top ~60 μm of the cross section. Monoliths of CeO_2 that experienced dissolution for several durations are shown in Figure 4b–d. After 7 days, grains and grain boundaries were clearly visible (Figure 4b), and after 14 days entire grains appeared to become separated from one another (Figure 4c). After 21 days of dissolution, the grains appeared to decrease considerably in size to ~5 μm, in agreement with the surface topography shown in Figure 3d; close inspection revealed that the grains were, in fact, fractured between pores, giving rise to apparently smaller grains. These data confirm that grain boundary dissolution in CeO_2 is extensive, and that grain boundaries may act as conduits for solution ingress, leading to dissolution and fracturing between pores. This process is expected to contribute substantially to the overall dissolution rate.

Analysis of the CeO_2 sample used to provide solution data at 90 °C, shown in Figure 1b, was performed using AFM and EBSD. Figure 5 shows the boundaries between several grains of different crystallographic orientation, including grain boundary "A" between surfaces of (025) and (001), and grain boundary "B" between surfaces of (001) and (356). EBSD analysis of these boundaries gave mean misorientation angles of 36.01° and 59.84°, respectively (Table 2). The dissolution of these boundaries was monitored over a period of 7 days (after which the surface became too rough to accurately measure) with reference to an inert surface mask of constant height. The mean surface retreat rates were measured as 0.001, 0.032, and 5.954 nm d^{-1} for the (025), (001), and (365) surfaces, respectively, indicating surface stability in the order: (025) < (001) < (365).

The retreat rates of CeO_2 grain boundaries were greater than the surface retreat rates between 0 and 1 days, and the retreat rate was different in different grain boundaries. Between 0 and 1 days of dissolution, the measured retreat of grain boundary A was 0.13 μm on the (025) aspect and 0.04 μm on the (001) aspect (Figure 5). Grain boundary B retreated more rapidly, increasing in depth by 0.21 μm on the (001) aspect, and 0.07

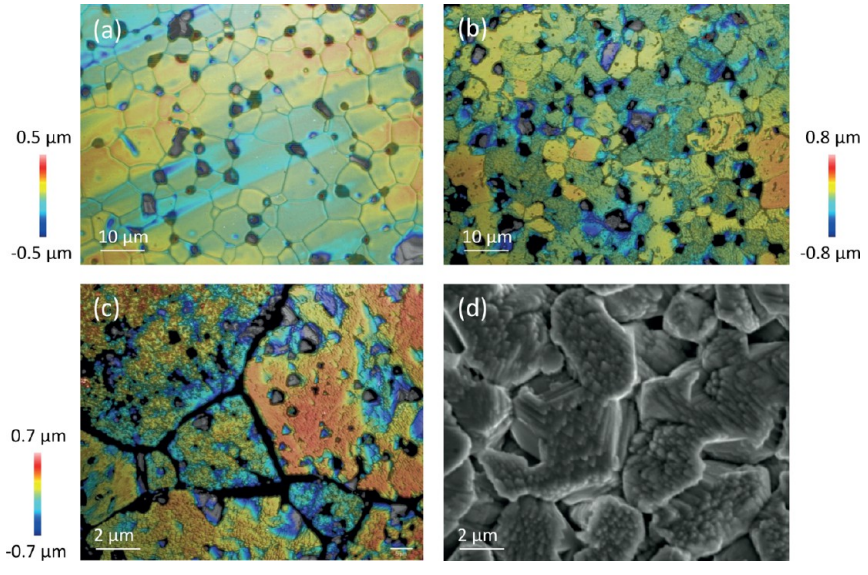

Figure 3. Vertical scanning interferometer and SEM images of CeO_2 surfaces (a) prior to dissolution and following dissolution for (b) 3 days, (c) 7 days, and (d) 21 days in 0.01 M HNO_3 at 150 °C.

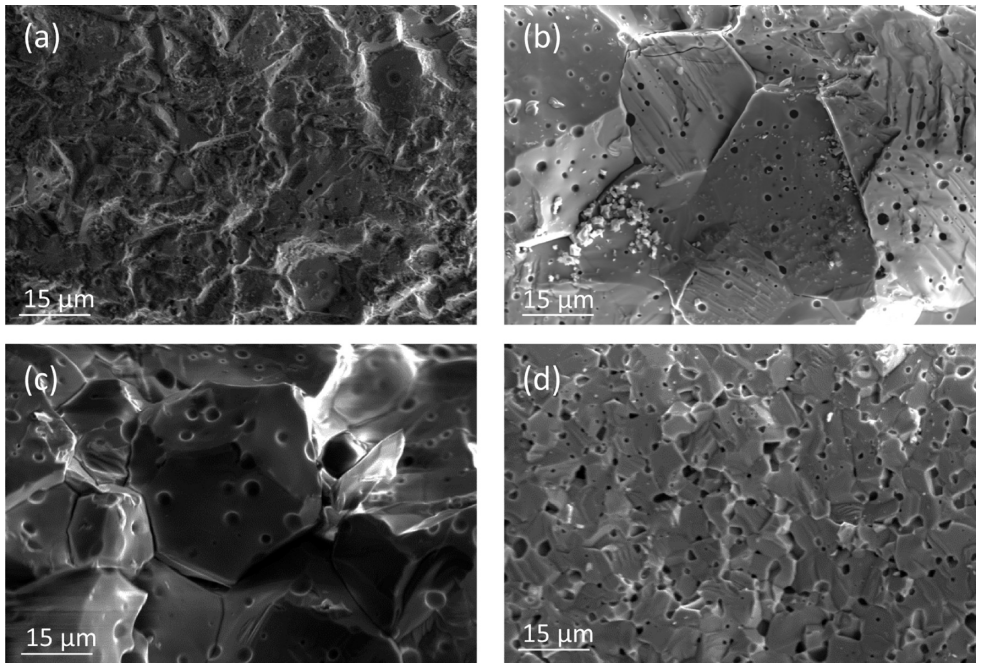

Figure 4. SEM images of cross sections through CeO_2, with the surface of the sample just above the top of each image: (a) nondissolved, annealed CeO_2; and CeO_2 dissolved in 0.01 M HNO_3 at 150 °C for (b) 7 days, (c) 14 days, and (d) 21 days.

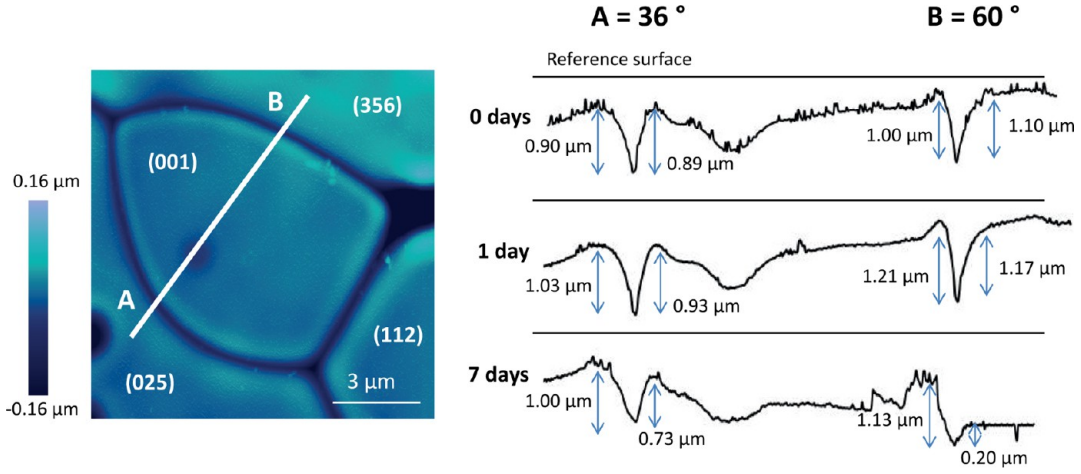

Figure 5. Atomic force microscopy image and cross sections of CeO_2 grains, with grain boundaries of low (A) and high (B) misorientation angles. Grain surfaces are measured against an inert reference surface of constant height. Cross sections show change in depth of the grain boundaries and grain surfaces with time, during dissolution at 90 °C in 0.01 M HNO_3.

Table 2. Grain Boundary Depths of CeO_2 (Corresponding to Figure 5) and ThO_2 Grains with Different Grain Orientations and Grain Boundary Misorientation Angles, as a Function of Time during Dissolution in 0.01 M HNO_3 at 90 °C

analogue composition	grain orientations	grain boundary misorientation angle (deg) (±0.01)	grain boundary depth (μm) 0 days (±0.01)	1 day (±0.01)	7 days (±0.01)	grain boundary retreat rate (μm d^{-1}) (±0.001)
CeO_2	(025)/(001)	36.01	0.90	1.03	1.00	0.014
	(001)/(356)	59.84	1.01	1.21	1.13	0.017
ThO_2	(103)/(506)	23.91	0.04	0.05	0.09	0.007
	(103)/(014)	39.33	0.06	0.14	0.15	0.012
	(416)/(506)	56.05	0.07	0.12	0.17	0.357

μm on the (356) aspect (Figure 5). Grain boundaries became deeper during dissolution, suggesting the removal of material from within. Furthermore, the dissolution was greatest for the high misorientation angle boundary, as compared to the low misorientation angle grain boundary, giving grain boundary retreat rates of 0.017 and 0.014 μm d^{-1}, respectively (Table 2). After 7 days of dissolution, grain boundaries appeared to become shallower as a result of enhanced grain surface retreat at this time, especially for grain boundary B where the (356) surface dissolved very rapidly (Figure 5). In summary, when

CeO_2 samples were contacted with the dissolution medium, a rapid loss of material from grain boundaries occurred, which is in agreement with the enhanced release of Ce into solution during this time (Figure 1a). Subsequently, surface retreat rates increased, and the surface, or matrix, dissolution became the dominant dissolution mechanism. Comparison to the aqueous Ce concentrations in Figure 1a shows that the dissolution was less rapid after 7 days, confirming that grain boundary dissolution contributes significantly to the initial dissolution rate, while surface controlled dissolution leads to slower dissolution rates.

Similar experiments were conducted to monitor the dissolution of ThO_2 grain boundaries as a function of crystallographic orientation and grain boundary misorientation using AFM and EBSD (Table 2). The dissolution behavior of ThO_2 grain boundaries at 90 °C in 0.01 M HNO_3 was comparable to that of CeO_2, whereby grain boundaries preferentially dissolved and boundaries with high misorientation angles retreated more rapidly than those with low misorientation angles. For example, a grain boundary between two grains with (103) and (506) surfaces had a misorientation angle of 23.91° and a retreat rate of 0.007 μm d^{-1}, while another grain boundary formed between grains with (416) and (506) surfaces with a mean misorientation angle of 56.05° gave a retreat rate of 0.357 μm d^{-1}, more than twice that of the lower misorientation angle grain boundary (Table 2). It should be noted that after 7 days of dissolution it was no longer possible to measure grain boundaries in ThO_2 due to the presence of a surface layer, giving further evidence to the hypothesis discussed above, that a dissolution rate drop after 7 days (Figure 1c) is due to the formation of a protective layer that results from the transformation of amorphous $ThO_x(OH)_y \cdot H_2O$ to $ThO_{2(cr)}$ precipitates.

3.3. Surface Facets. Surface facets comprising flat terraces separated by inclined steps were found on annealed grains of CeO_2 (Figure 2). These features were not observed on ThO_2 because of its increased surface roughness, produced by difficulties encountered in polishing the sample. EBSD analysis of these grains was not possible due to multiple orientations arising from the faceted surfaces; however, alternative geometric measurements were used to determine the orientation of the facet features. By measuring the angle, θ, between the facet and the surface, the best combination of planes can be found according to Maldonado et al.:[25]

$$\theta = \arccos\left(\frac{\vec{u}\cdot\vec{v}}{|\vec{u}||\vec{v}|}\right) \quad (3)$$

where $\vec{u}$ and $\vec{v}$ are the normal vectors that define the planes. Godinho et al.[23] showed that a dissolution surface is only made of the most stable planes, as the less stable ones are more prone to dissolution. Therefore, if we assume only the most stable planes are present at the surface, this method allows the unambiguous definition of the intersection of two distinct planes. Figure 6 illustrates this concept, showing the lateral view of a hypothetical surface comprised of two planes. These planes are the {111} and {100} planes, which intersect forming a facet with an angle θ = 70.52°/109.48°.

Several different planar orientations of surface facets were observed. Grain "A" in Figure 2 exhibited regularly stepped facets across the surface of the grain, while grain "B" developed facets that increased in height from the center of the grain to the edge. According to den Brok and Morel,[26] these ridge and valley features result from elastic strain released during annealing, lowering the surface energy. Some grains, for example, grain "C" (Figure 2), showed no facets. The facets on grain "A" enclosed an angle of 106.83 ± 2.1°, indicative of a {665}/{$\bar{1}$11} plane intersection, which is known to have an angle of 107.04°. The height of these facets ranged from 4.66 to 16.71 nm, and the flat terraces between facets were consistently separated by distances of 5.74 nm. The facets on grain "B" (Figure 2) had planar orientations that met at an angle of 110.33 ± 1.6°, indicative of a {111}/{$\bar{1}$11} facet orientation, which has a known angle of 109.47°. These facets ranged in height from 1.50 to 6.61 nm and had flat terraces of 24.06 nm (or multiples thereof). These {111}/{$\bar{1}$11} facets were themselves faceted, giving rise to a "zigzag" edge, as shown in Figure 7a. These "mini-facets" were found to be perpendicular to the {$\bar{1}$11} plane, suggestive of the plane {511}. The facet structures were also observed to extend into the grain boundaries (Figure 7b). Figure 7b–e shows detailed AFM images of another grain, which exhibited a ridge and valley-like morphology, with stacked concentric facets, building ridges at the grain edges (giving rise to the "tooth-shaped" grains shown in AFM profiles in Figure 5) and flat valleys in the center of the grain. The difference in height between the ridges and valleys for this grain was up to 150.36 nm. The facet heights ranged from 2.50 to 58.04 nm, were unevenly spaced at distances <20.02 nm, and enclosed an angle 125.43 ± 0.7°. This is indicative of a {111}/{100} planar orientation, which has a known angle of 125.26°. It can be noted that all of the facets found at the surface of CeO_2 involve the most stable plane, {111}.

To understand the dissolution of the CeO_2 surface facets, samples were subjected to high acidity (pH <2) dissolution experiments. The surface shown in Figure 7b–e was subject to dissolution at room temperature in increasing concentrations of nitric acid, representing increasingly aggressive dissolution conditions. The resulting facet height measurements, corresponding to the facets between point 1 and point 8, shown in Figure 7e, are given in Table 3. It is clear that the addition of just 0.01 M HNO_3 resulted in a significant increase in height for most facets, as compared to the height prior to dissolution. Facet height increases ranged between 1.30 and 3.91 nm. Two facets were observed to become shallower (facets 2 and 5, Table 3). With increasing acidity between 0.1 and 3 M HNO_3, facet height change was variable, with some facets showing little change (Table 3), while others decreased in height and others increased (suggesting addition of material to facets). This variability suggests that these surface sites are highly dynamic, changing in response to the reaction medium, but with little observable trend. However, it is clear that upon initial immersion in the reaction medium, instantaneous dissolution of the facets occurred.

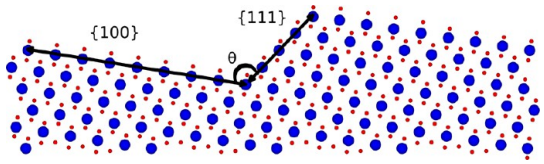

Figure 6. Lateral view of a hypothetical CeO_2 surface (large blue dots are O, small red dots are Ce), composed of the {100} and {111} surfaces, intersecting at an angle, θ, of 70.52°/109.48° (rendered by VESTA).

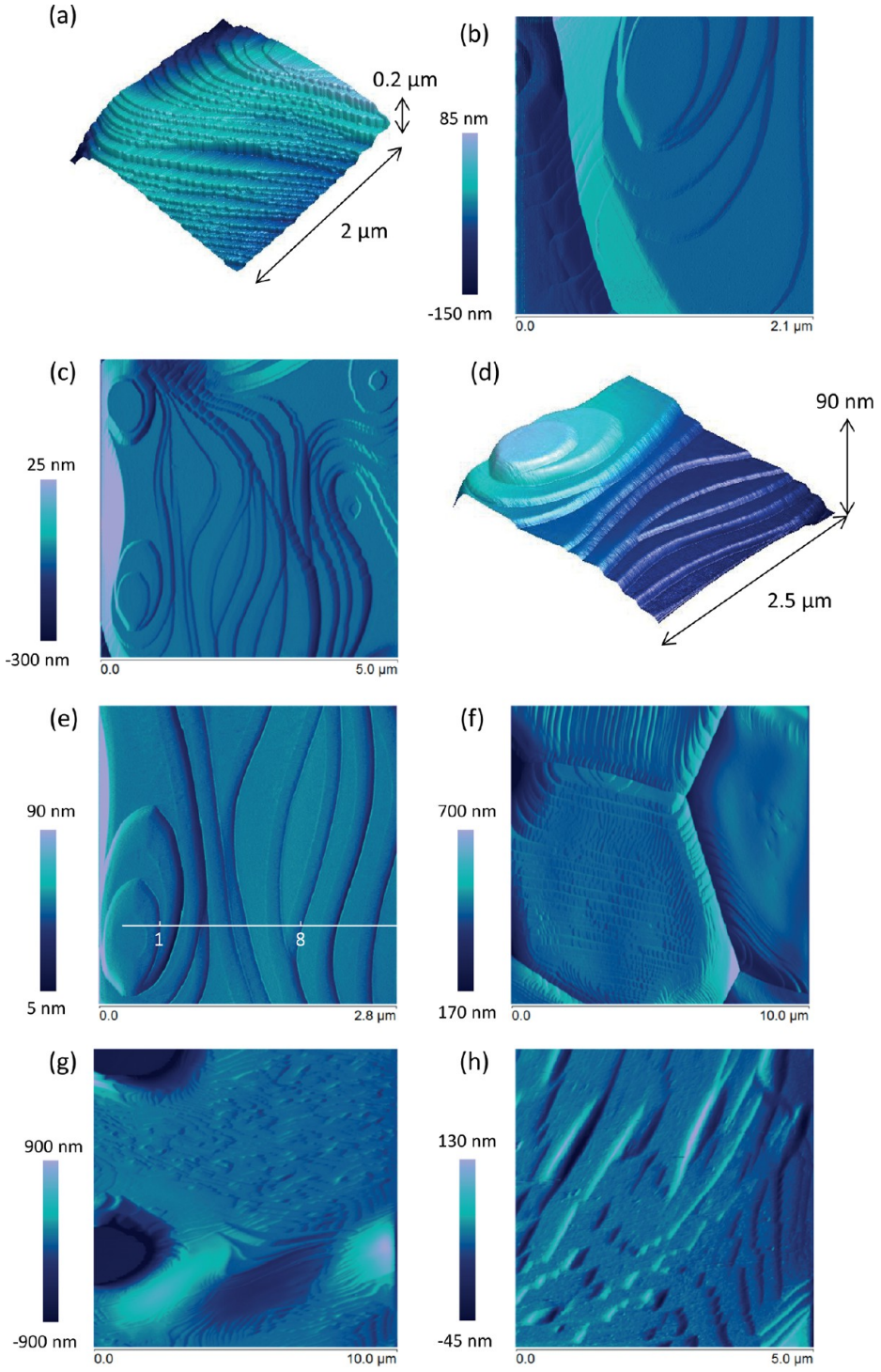

Figure 7. Atomic force microscopy images depicting surface features of CeO_2 spent nuclear fuel analogue surfaces: (a) showing $\{\bar{2}11\}$ microfacets perpendicular to the plane $\{\bar{1}11\}$; (b) facet structures extending into grain boundaries; (c) ridge and valley structure formed by intersecting {111}/{100} planes; (d and e) intersecting {111}/{100} planes showing cross section for step height measurements in Table 3; (f) $\{\bar{2}11\}/\{\bar{1}11\}$ surface facets following dissolution in 15 M nitric acid at room temperature; and (g and h) etch pattern formed on previously smooth grains following etching in a series of media (UHQ water for 72 h, 0.001 M for 15 h, and 0.01 M HCl for 4 h) at room temperature. Images (a), (g), and (h) were taken in air, and all remaining images were taken in solution.

To investigate the effect of dissolution on the {511} microfacets perpendicular to the $\{\bar{1}11\}$ plane (grain "B", Figure 2 and Figure 7a), a grain with these features was subject to dissolution in a 15 M HNO_3 solution at room temperature. The resulting surface is shown in Figure 7f. The effect of dissolution was increased microfacetting in the {511} plane. Even under these aggressive conditions, it was not possible to see any change in the smooth grains; therefore, the samples were etched in a series of media for a prolonged period (72 h in UHQ water, 15 h in 0.001 M HCl, and 4 h in 0.01 M HCl) at room temperature. The resulting AFM images show that the smooth grain became highly etched, forming "zigzag" features

dx.doi.org/10.1021/am5018978 | ACS Appl. Mater. Interfaces 2014, 6, 12279−12289

Table 3. Facet Heights Measured from Figure 7e as a Function of HNO_3 Molarity

	facet height (nm) (±0.01)							
nitric acid concn (M)	facet 1	facet 2	facet 3	facet 4	facet 5	facet 6	facet 7	facet 8
none	5.83	1.81	2.55	0.94	2.85	2.75	1.12	0.25
0.01	8.53	1.20	4.70	1.43	1.69	6.94	2.95	3.92
0.1	8.50	1.56	2.07	3.80	0.04	5.68	2.68	3.14
1.5	7.92	1.01	3.00	2.00	0.06	7.23	1.87	2.64
3	9.68	1.14	2.91	2.76	0.03	6.97	1.05	1.37

and triangular points (Figure 7g,h). Each etched layer was separated by steps, which were 30.01 nm in height (or multiples thereof). Triangular facets have been observed previously in etched CaF_2,[27] forming lightening-shaped arrangements of intersecting (101) and (110) facets.

3.4. Surface Treatment. High energy surface sites may also be induced through specimen preparation, leading to overestimated laboratory dissolution rates. Surfaces of CeO_2 were polished to a 0.05 μm finish and subject to dissolution at 150 °C in 0.01 M HNO_3. Dissolution data were compared to those for annealed surfaces. Figure 8 shows VSI images of the surface

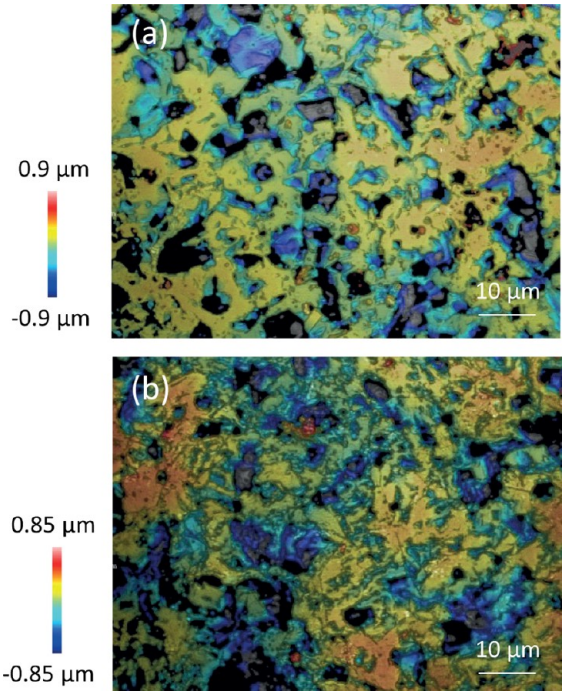

Figure 8. Polished CeO_2 surfaces after dissolution in 0.01 M HNO_3 at 150 °C for (a) 3 days and (b) 14 days.

of a polished monolith after 3 and 14 days of dissolution (Figure 8a,b, respectively). During initial dissolution, the surfaces were rough and pitted, and after 14 days exhibited areas of high and low topography, indicating further dissolution had occurred. It was found that the dissolution rate was an order of magnitude greater for the polished surface than for an annealed CeO_2 surface under the same conditions (Table 2). At 90 °C, the effect was similar; however, the dissolution rate of the polished surface was found to be 3 orders of magnitude greater than that of an annealed surface, with rates of $(7.40 \pm 0.2) \times 10^{-2}$ and $(7.26 \pm 0.2) \times 10^{-5}$ g m^{-2} d^{-1} for polished and annealed surfaces, respectively (Table 1).

4. DISCUSSION

In the results presented above, we have observed that surface features act as energetically reactive surface sites that transform during dissolution. These features can be classified into two categories: (i) natural surface features, that is, grain boundaries; and (ii) specimen preparation-induced features, that is, surface facets and polishing defects. The dissolution of these features in CeO_2 and ThO_2 is discussed below, with comparison to the dissolution behavior of UO_2. It should be noted that while the chemical and redox characteristics of the analogue materials investigated here are simple when compared to those of spent fuel, it is possible to draw comparisons between CeO_2, ThO_2, and spent fuel that focus only on the physical and structural properties that give rise to the dissolution behavior observed. As such, in the discussion that follows, only microstructural surface features that affect dissolution are described, with a cautious interpretation for the overall behavior of spent fuel during dissolution.

4.1. Grain Boundary Dissolution. The results presented in this investigation give evidence that UO_2 and spent nuclear fuel analogue grain boundaries undergo extensive transformation during dissolution; material is rapidly removed from grain boundaries in both CeO_2 and ThO_2, corresponding to rapid initial dissolution rates. It is hypothesized that grain boundaries are effective sinks for atomic defect high energy sites;[28] the greater the number of defects, the greater the proportion of high energy surface sites for dissolution. In CeO_2, it has been shown that increasing the density of oxygen vacancy defects results in an increase in the dissolution rate. For example, Horlait et al.[29,30] showed that for every 10% of Ln^{3+} cations added to CeO_2, for which charge compensation through the formation of Ce^{3+} occurred, the dissolution rate increased by 1 order of magnitude.[28] Hojo et al.[31] demonstrated an enrichment of Ce^{3+} in grain boundaries as compared to the grain surfaces, indicative of a higher density of oxygen vacancy defects within the grain boundaries as compared to the surface. In UO_2, evidence for defects within grain boundaries is found in the form of nonstoichiometric UO_{2+x}. For example, Une and Kashibe[32] identified the presence of $UO_{2.25}$ within grain boundaries following dissolution of UO_2, while O'Neil et al.[17] made the observation that grain boundaries in UO_2 were highly conductive, which was attributed to a high concentration of oxygen interstitial ions arising from hypo-stoichiometric UO_{2+x}. This suggests that defects, and especially those that are concentrated within grain boundaries, may play a key role in the dissolution of UO_2 and its analogues. In spent fuel, grain boundaries are expected to contain more defects than laboratory-prepared UO_2 or UO_2 analogues, primarily due to the accumulation of fission gas bubbles and metallic precipitates;[33] therefore, the effects of such high energy surface sites might be expected to be greater.

We have observed that crystallographic orientation of the grains plays an important role in the dissolution of the grain boundaries of spent nuclear fuel analogues; grain boundaries with a high misorientation angle were found to dissolve more rapidly than those with a low misorientation angle in the current study. We hypothesize that high misorientation grain boundaries have a higher concentration of defects (or defect clusters) than grain boundaries with low misorientation angles. Indeed, simulations of UO_2 grain boundaries have shown that different types of defect structure were present in grain boundaries, depending on the misorientation angle;[34] in grain boundaries with lower misorientation angles, edge dislocations were the most common defect, while in higher misorientation angle boundaries, oxygen point defects dominated the grain boundary structure.

Assessment of the safety of geological disposal of spent nuclear fuel requires detailed information on the rates and mechanism of release of radionuclides. This is hypothesized to occur in two main stages: (ii) the so-called "instant release fraction" (IRF), which represents a rapid release of long-lived and geochemically mobile radionuclides (e.g., ^{129}I, ^{36}Cl, ^{135}Cs, ^{99}Tc); and (ii) the slow, long-term release of radionuclides from the UO_2 matrix.[35,36] The IRF is considered to come from two regions of the spent fuel: the gap between the cladding and the fuel, and the grain boundaries. However, the IRF rates are still largely unknown, and the contribution of grain boundary dissolution is not fully understood; in fact, there is some controversy in the literature as to whether grain boundaries make any significant contribution to the IRF.[36,37] The results presented in the current work, which demonstrate an "instant release fraction" of Ce and Th from the spent fuel analogues, which is directly linked to grain boundary dissolution, support the hypothesis that grain boundaries contribute to the IRF in spent fuel, and suggest that crystallographic direction of the grains and the density of defects within the grain boundary may play a role. However, it should be noted that the IRF of spent fuel is largely governed by the complicated chemical composition of the grain boundaries; therefore, the extent to which structural defects and grain boundary misorientation between adjacent grains contribute to the IRF is unknown in comparison to the chemical effects. Our results are also in agreement with the hypothesis that a second, slower stage of spent fuel dissolution occurs; in both CeO_2 and ThO_2, dissolution rates were lower after the initial release. In ThO_2 it was apparent that this second stage of dissolution was impeded by the formation of a protective layer. A similar effect was found in laboratory UO_2 dissolution experiments, where secondary U-bearing alteration products formed a protective layer, preventing further dissolution.[38] On the basis of the data and arguments presented here, it is evident that grain boundary dissolution in spent fuel and spent fuel analogues requires further detailed chemical and physical analysis and that geological disposal safety performance assessment should carefully consider the contribution of grain boundaries to the dissolution rate.

4.2. Dissolution of Specimen Preparation-Induced Features. We show that dissolution occurs at facet edges, especially during initial contact with dissolution medium. With increasingly aggressive dissolution media, the dissolution of these features does not show a particular trend, but instead appears to experience a dynamic process, whereby facet heights constantly change in response to the dissolution medium. We have also shown that each facet contains some aspect of the {111} plane, which is the most stable plane in fluorite-type structures, suggesting that crystallographic orientation also plays an important role in facet formation.

It is thought that facets form by a dislocation growth mechanism during annealing, where spiral-like structures form around threading dislocations likely induced through surface preparation (e.g., polishing). Each dislocation produces a step as it emerges at the surface.[39,40] O'Neil et al.[17] and He and Shoesmith[40] described surface morphologies similar to those identified in the current study in UO_2. Current-sensing AFM analysis showed that UO_2 grains with facets were highly conducting, while smooth grains were not. Raman and EDX investigation of these features revealed a high degree of nonstoichiometry in the UO_2 of faceted grains, attributed to the incorporation of interstitial oxygen atoms to locations in the {110} direction, accompanied by shifts in vacant sites in the {111} direction. It was concluded that these nonstoichiometric, defect-containing features would be more vulnerable to dissolution than defect-free surfaces. Further investigations are currently underway to understand the relative stability of different facet orientations, their degree of nonstoichiometry, and defect structures. It is clear that these high energy surface sites play a role in dissolution, but the evidence presented here suggests that the influence on dissolution rate is not as significant as that of grain boundaries. It is important to note that these features are present as a result of specimen preparation and annealing, and thus are likely to contribute to the potential overestimation of dissolution rates in the laboratory. These features are not expected to be present in spent nuclear fuel.

We found that polished surfaces of spent nuclear fuel analogues gave dissolution rates of up to 3 orders of magnitude greater than for annealed surfaces. Polishing has been shown to introduce strain and defects into oxide material surfaces, giving rise to high surface energy. For example, diamond paste polishing has been shown to result in the formation of dislocation loops, other lattice defects, and also high surface strain.[41,42] Thermally annealing the surface of CeO_2 allowed the strain and defects to be relaxed due to recovery processes during heating, lowering the surface energy, and thus lowering the dissolution rate. It is possible that defects induced during polishing may act as nucleation sites for the observed facet structures formed during annealing. These results show that the introduction of defects to the surface through polishing can lead to a significant increase in the observed dissolution rate, demonstrating the importance of careful specimen preparation for dissolution rate determination.

5. CONCLUSIONS

Dissolution experiments were conducted on non-redox sensitive, isostructural UO_2 and SNF analogues, CeO_2 and ThO_2, to investigate the contribution of energetically reactive surface sites to dissolution, and to determine whether their presence may lead to an overestimation of dissolution rates. Grain boundaries, which are part of the natural texture of SNF, were shown to significantly enhance the dissolution rate, dissolving preferentially in the initial stages of dissolution, supporting hypotheses that grain boundaries contribute to the instant release fraction of spent fuel. A strong crystallographic control was exerted, with high misorientation grain boundaries dissolving more rapidly than those with low misorientation angles in both CeO_2 and ThO_2. It was hypothesized that different crystallographic directions can accommodate different

densities of defects, explaining the observations found. Further investigation is required to ascertain the extent to which structural defects and grain boundary misorientation between adjacent grains contribute to the instant release fraction of SNF, in comparison to the chemical effects.

In addition to the natural high energy surface sites found in grain boundaries, energetically reactive sites were also found to be formed through sample preparation. Facet structures formed during annealing, likely nucleated on defects sites on polished surfaces, also exhibited a strong crystallographic control (all combined some aspect of the {111} plane), and upon introduction to dissolution media, they experienced instantaneous dissolution. Finally, the effect of surface polishing on the dissolution rate was found to increase dissolution rates by up to 3 orders of magnitude. This results from induction of strain and defects in the surface during the polishing process. We have shown that defects induced through sample preparation contribute to the dissolution rate. The dissolution from facets is low, and therefore not likely to significantly overestimate long-term dissolution rates; however, sample polishing without any further treatment is likely to cause overestimation of dissolution rates.

AUTHOR INFORMATION

Corresponding Authors

*Tel.: +44 (0)1142226036. E-mail: c.corkhill@sheffield.ac.uk.
*Tel.: +44 (0)1142224570. E-mail: n.c.hyatt@sheffield.ac.uk.

Notes

The authors declare no competing financial interest.

ACKNOWLEDGMENTS

The research leading to these results has received funding from the European Atomic Energy Community's Seventh Framework Programme (FP7) under grant agreement no. 269903, The REDUPP (REDucing Uncertainty in Performance Prediction) project. Special thanks goes to J. Godinho for assistance with vertical scanning interferometry. We are grateful to Dr. Virginia Oversby and Dr. Lena Z. Evins for invaluable discussion and support throughout the project. C.L.C. is grateful to The University of Sheffield for the award of a Vice Chancellor's Fellowship, N.C.H. acknowledges support from the Royal Academy of Engineering and the Nuclear Decommissioning Authority for funding, and D.J.B. and S.M.T. acknowledge financial support from the EPSRC Nuclear FiRST Doctoral Training Centre (EP/G037140/1). We are grateful to the anonymous reviewers of this contribution, for their insightful comments and suggestions, which have greatly improved the manuscript.

REFERENCES

(1) Oversby, V. M. Uranium Dioxide, SIMFUEL and Spent Fuel Dissolution Rates – A Review Of Published Data. *SKB Tech. Rep.*, 1999, TR-99-22.

(2) Shoesmith, D. W. Used Fuel and Uranium Dioxide Dissolution Studies – A Review. *Nucl. Waste Manage. Org. Rep.* **2007**, NMWO TR-2007-03.

(3) Fuel and Canister Process Report for the Safety Assessment SR-Site. *SKB Tech. Rep.*, 2010, TR-10-46.

(4) Smellie, J.; Karlson, F. A Reappraisal of some Cigar Lake Issues of Importance to Performance Assessment. *SKB Tech. Rep.*, 1996, TR 96-08.

(5) Gauthier-Lafaye, F.; Holliger, P.; Blanc, P. L. Natural Fission Reactors in the Franceville Basin, Gabon: A Review of the Conditions and Results of a "Critical Event" in a Geologic System. *Geochim. Cosmochim. Acta* **1996**, *60*, 4831–4852.

(6) Knauss, P.; Wolery, T. J. Dependence of Albite Dissolution Kinetics on pH and Time at 25 °C and 70 °C. *Geochim. Cosmochim. Acta* **1986**, *50*, 2481–2497.

(7) White, A. F.; Bullen, T. D.; Schulz, M. S.; Blum, A. E.; Huntington, T. G.; Peters, N. E. Differential Rates of Feldspar Weathering in Granitic Regoliths. *Geochim. Cosmochim. Acta* **2001**, *65*, 847–867.

(8) White, A. F.; Brantley, S. L. The Effect of Time on the Weathering of Silicate Minerals: Why do Weathering Rates Differ in the Laboratory and Field? *Chem. Geol.* **2003**, *202*, 479–506.

(9) Zhu, C.; Veblen, D. R.; Blum, A. E.; Chipera, S. J. Naturally Weathered Feldspar Surfaces in the Navajo Sandstone Aquifer, Black Mesa, Arizona: Electron Microscopic Characterisation. *Geochim. Cosmochim. Acta* **2006**, *70*, 4600–4616.

(10) Brantley, S. L.; Crane, S. R.; Creear, D.; Hellmann, R.; Stallard, R. Dissolution at Dislocation Edge Pits in Quartz. *Geochim. Cosmochim. Acta* **1986**, *50*, 2349–2361.

(11) Blum, A. E.; Lasaga, A. C. Monte Carlo Simulations of Surface Reaction Rate Laws. In *Chemical Weathering Rates of Silicate Minerals*; Stumm, W., Ed.; Mineralogical Society of America: 1987; Vol. *31*, pp 291–351.

(12) Ollila, K.; Oversby, V. M. Dissolution of Unirradiated UO_2 and UO_2 Doped with ^{233}U Under Reducing Conditions. *SKB Tech. Rep.*, 2005, TR-05-07.

(13) Ollila, K. Dissolution of Unirradiated UO_2 and UO_2 Doped with ^{233}U in 0.01M NaCl Under Anoxic and Reducing Conditions. *Posiva Oy Rep.* **2006**, 2006–08.

(14) Claparede, L.; Clavier, N.; Dacheux, N.; Moisy, N.; Podor, R.; Ravaux, J. Influence of Crystallisation State and Microstructure on the Chemical Durability of Cerium-Neodymium Mixed Oxides. *Inorg. Chem.* **2011**, *50*, 9059–9072.

(15) Stennett, M. C.; Corkhill, C. L.; Marshall, L. A.; Hyatt, N. C. Preparation, Characterisation and Dissolution of a CeO_2 Analogue for UO_2 Nuclear Fuel. *J. Nucl. Mater.* **2013**, *432*, 182–188.

(16) Evins, L. Z.; Juhola, P.; Vahanen, M. REDUPP Final Report. *Posiva Oy Rep.* **2014**, 2014–12.

(17) O'Neil, K. D.; He, H.; Keech, P.; Shoesmith, D. W.; Semenikhin, O. A. Anisotropy of Local Conductivity of Hyper-Stoichiometric Uranium Dioxide Revealed by Current-Sensing Atomic Force Microscopy (CS-AFM). *Electrochem. Commun.* **2008**, *10*, 1805–1808.

(18) Lucuta, P. G.; Verall, V. R.; Maztke, Hj.; Palmer, B. J. Microstructural Features of SIMFUEL – Simulated High-Burnup UO_2-Based Nuclear Fuel. *J. Nucl. Mater.* **1991**, *178*, 48–60.

(19) Papin, P.; Chen, C.-F.; Forsyth, R.; Luther, E.; Necker, C. Surface Preparation for Characterising Microstructure on Transuranic Oxides by Electron Backscatter Spectroscopy and Ion Beam Imaging. *Microsc. Microanal.* **2012**, *18*, 708.

(20) ASTM. *Standard Test Methods for Determining Chemical Durability of Nuclear, Hazardous and Mixed Waste Glasses and Multiphase Ceramics: The Product Consistency Test (PCT)*; ASTM C 1285-02; American Society for Testing and Materials: Philadelphia, PA, 2008.

(21) Rai, D.; Moore, D. A.; Oakes, C. S.; Yui, M. Thermodynamic Model for the Solubility of Thorium Dioxide in the Na-Cl-OH-H_2O System at 23 °C and 90 °C. *Radiochim. Acta* **2000**, *88*, 297–306.

(22) Cui, D.; Low, J.; Spahiu, K. Environmental Behaviours of Spent Nuclear Fuel and Canister Materials. *Energy Environ. Sci.* **2011**, *4*, 2537–2545.

(23) Godinho, J.; Piazolo, S.; Evins, L. Z. Effect of Surface Orientation on Dissolution Rates and Topography of CaF_2. *Geochim. Cosmochim. Acta* **2012**, *86*, 392–403.

(24) Yang, Z.; Woo, T. K.; Baudin, M.; Hermannsson, K. Atomic and Electronic Structure of Unreduced and Reduced CeO_2 Surfaces: A First-Principles Study. *J. Chem. Phys.* **2004**, *120*, 7741–7749.

(25) Maldonado, P.; Godinho, J.; Evins, L. Z.; Oppeneer, P. M. Ab initio Prediction of Surface Stability of Fluorite Materials and Experimental Verification. *J. Phys. Chem. C* **2013**, *117*, 6639–6650.

(26) den Brok, S. W. J.; Morel, J. The Effect of Elastic Strain on the Microstructure of Free Surfaces of Stressed Minerals in Contact with an Aqueous Solution. *Geophys. Res. Lett.* **2001**, *28*, 603−606.
(27) Englehardt, J. B.; Dabringhaus, H.; Wandelt, K. Atomic Force Microscopy Study of the CaF_2 (111) Surface: From Cleavage via Island to Evaporation topographies. *Surf. Sci.* **2000**, *448*, 187−200.
(28) Horlait, D.; Claparede, L.; Tocino, F.; Clavier, N.; Ravaux, J.; Szenknect, S.; Podor, R.; Dacheux, N. Environmental SEM Monitoring of $Ce_{1-x}Ln_xO_{2-x/2}$ Mixed-Oxide Microstructural Evolution During Dissolution. *J. Mater. Chem. A* **2014**, DOI: 101039/c3ta14623e.
(29) Horlait, D.; Clavier, N.; Szenknect, S.; Dacheux, N.; Dubois, V. Dissolution of Cerium(IV)- Lanthanide(III) Oxides: Comparative Effect of Chemical Composition, Temperature, and Acidity. *Inorg. Chem.* **2012**, *51*, 3868−3878.
(30) Horlait, D.; Tocino, F.; Clavier, N.; Dacheux, N.; Szenknect, S. Multiparametric Study of $Th(_{1-x})Ln(_x)O(_{2-x/2})$ Mixed Oxides Dissolution in Nitric Acid Media. *J. Nucl. Mater.* **2012**, *429*, 237−244.
(31) Hojo, H.; Mizoguchi, T.; Ohta, H.; Findlay, S. D.; Shibata, N.; Yamamoto, T.; Ikuhara, Y. Atomic Structure of a CeO_2 Grain Boundary: The Role of Oxygen Vacancies. *Nano Lett.* **2010**, *10*, 4668−4672.
(32) Une, K.; Kashibe, S. Corrosion Behaviour of Irradiated Oxide Fuel Pellets in High Temperature Water. *J. Nucl. Mater.* **1996**, *232*, 240−247.
(33) Marchetti, I.; Carbol, P.; Himbert, J.; Belloni, F.; Fanghanel, T. Room-Temperature Diffusion Coefficients for Oxygen and Water in UO_2 Matrices: A SIMS Study. *Surf. Interface Anal.* **2013**, *45*, 360−363.
(34) Van Brutzel, L.; Vincent-Aublant, E. Grain Boundary Influence on Displacement Cascades in UO_2: A Molecular Dynamics Study. *J. Nucl. Mater.* **2008**, *377*, 522−527.
(35) Johnson, L. H.; Tait, J. C. Release of Segregated Radionuclides from Spent Fuel. *SKB Tech. Rep.*, 1997, TR-97-18.
(36) Johnson, L.; Gunther-Leopold, I.; Kobler Waldis, J.; Linder, H. P.; Low, J.; Cui, D.; Ekeroth, E.; Spahiu, K.; Evins, L. Z. Rapid Aqueous Release of Fission Products from High Burn-Up LWR Fuel: Experimental Results and Correlations with Fission Gas Release. *J. Nucl. Mater.* **2012**, *420*, 54−62.
(37) Serrano-Purroy, D.; Clarens, F.; Gonzalez-Robles, E.; Glatz, J. P.; Wegen, D. H.; de Pablo, J.; Casas, I.; Gimenez, J.; Martinez-Esparza, A. Instant Release Fraction and Matrix Release of High Burn-Up UO_2 Spent Nuclear Fuel: Effect of High Burn-Up Structure and Leaching Solution Composition. *J. Nucl. Mater.* **2012**, *427*, 249−258.
(38) Wronkiewicz, D. J.; Buck, E. C.; Bates, J. K. Grain Boundary Corrosion and Alteration Phase Formation During the Oxidative Dissolution of UO_2 Pellets. *Mater. Res. Soc. Symp. Proc.* **1997**, *465*, 519.
(39) Schick, M.; Dabringhaus, H.; Wandelt, K. Macrosteps on CaF_2 (111). *J. Phys.: Condens. Matter* **2004**, *16*, L33−L37.
(40) He, H.; Shoesmith, D. W. Raman Spectroscopic Studies of Defect Structures and Phase Transition in Hyper-Stoichiometric UO_{2+x}. *Phys. Chem. Chem. Phys.* **2010**, *12*, 8108−8117.
(41) Johansson, S.; Schweitz, J.; Lagerlof, K. P. D. Surface Defects in Polished Silicon Studies by Cross-Sectional Transmission Electron Microscopy. *J. Am. Ceram. Soc.* **1989**, *72*, 1136−1139.
(42) Saito, T.; Hirayama, T.; Yamamoto, T.; Ikuhara, Y. Lattice Strain and Dislocations in Polished Surfaces on Sapphire. *J. Am. Ceram. Soc.* **2005**, *88*, 2277−2285.